nature communications

Article

https://doi.org/10.1038/s41467-025-57904-5

Controlling outer-sphere solvent reorganization energy to turn on or off the function of artificial metalloenzymes

Received: 28 July 2024

Accepted: 5 March 2025

Published online: 28 March 2025

Check for updates

Divyansh Prakash[1,3], Suchitra Mitra[1,4], Simran Sony[1], Morgan Murphy[1], Babak Andi[2], Landon Ashley[1], Pallavi Prasad[1,5] & Saumen Chakraborty[1]

Metalloenzymes play essential roles in biology. However, unraveling how outer-sphere interactions can be predictably controlled to influence their functions remains a significant challenge. Inspired by Cu enzymes, we demonstrate how variations in the primary, secondary, and outer coordination-sphere interactions of de novo designed artificial copper proteins (ArCuPs) within trimeric (3SCC) and tetrameric (4SCC) self-assemblies—featuring a trigonal $Cu(His)_3$ and a square pyramidal $Cu(His)_4(OH_2)$ coordination—influence their catalytic and electron transfer properties. While 3SCC electrocatalyzes C-H oxidation, 4SCC does not. Cu^{I}-3SCC reacts more rapidly with H_2O_2 than O_2, whereas 4SCC is less active. Electron transfer, reorganization energies, and extended H_2O-mediated hydrogen bonding patterns provide insights into the observed reactivity differences. The inactivity of 4SCC is attributed to a significant solvent reorganization energy barrier mediated by a specific His---Glu hydrogen bond. When this hydrogen bond is disrupted, the solvent reorganization energy is reduced, and C-H peroxidation activity is restored.

Redox-active metalloenzymes possess optimized primary, secondary, and outer-sphere interactions to control catalysis and electron transfer (ET)[1–5]. The active site minimizes oxidation state-dependent structural changes, which lowers the reorganization energy (λ), facilitating ET and catalysis. The coordination number, geometry, and protein matrix are critical determinants facilitating redox catalysis. Copper (Cu)--containing metalloproteins are at the heart of numerous biochemical processes, such as respiration, ET, biomass degradation, hydrocarbon oxidation, and the biosynthesis of hormones and cofactors[1,6,7]. The type-1 Cu centers are involved only in ET, but the type-2 Cu proteins can participate in ET or catalysis[1,6]. Cu is predominantly found in a 3-5 coordinate geometry with S, N, and O-containing ligands such as Cys, Met, His, terminal amine, Asp/Asn, Tyr, or water. Amine oxidase (AO)[8], nitrite reductase (NiR)[9], and the Cu_B site of cytochrome c oxidase (CcO)[10] feature a $Cu(His)_3$ ligation (Fig. 1A, B), also found in the coupled binuclear active site of tyrosinase (Ty). The lytic polysaccharide monooxygenases (LPMOs) have a T-shaped $Cu(His)_2NH_2$ geometry formed by a His-brace (Fig. 1C)[11–15]. In addition to O_2, LPMOs can utilize H_2O_2 to oxidatively depolymerize recalcitrant cellulosic substrates, causing them to be designated as peroxygenases [16–21].

Particulate methane monooxygenases (pMMOs) are membrane-bound enzymes initially thought to feature a bimetallic Cu-Cu active site[22,23]. However, based on recent structural and EPR studies, pMMOs are now considered to contain only mono-copper active sites[24–27]. The membrane-bound Cu_C or the Cu_D site is the proposed active site where O_2 binding and CH_4 oxidation occur[25–27]. Another Cu site, Cu_B, located in the soluble PmoB subunit, has a unique square pyramidal $Cu(His)_3(NH_2)(OH_2)$ coordination from 3 His, a terminal amine, and axial water (Fig. 1D). Although not the hydrocarbon binding site, the Cu_B site is important since deleting Cu_B ligands in homologous

[1]Department of Chemistry and Biochemistry, University of Mississippi, University, MS, USA. [2]Center for BioMolecular Structure, National Synchrotron Light Source II, Brookhaven National Laboratory, Upton, NY, USA. [3]Present address: Northwestern University, Evanston, IL, USA. [4]Present address: Weill Cornell Medicine, New York, NY, USA. [5]Present address: Regeneron Pharmaceuticals, Tarrytown, NY, USA. e-mail: saumenc@olemiss.edu

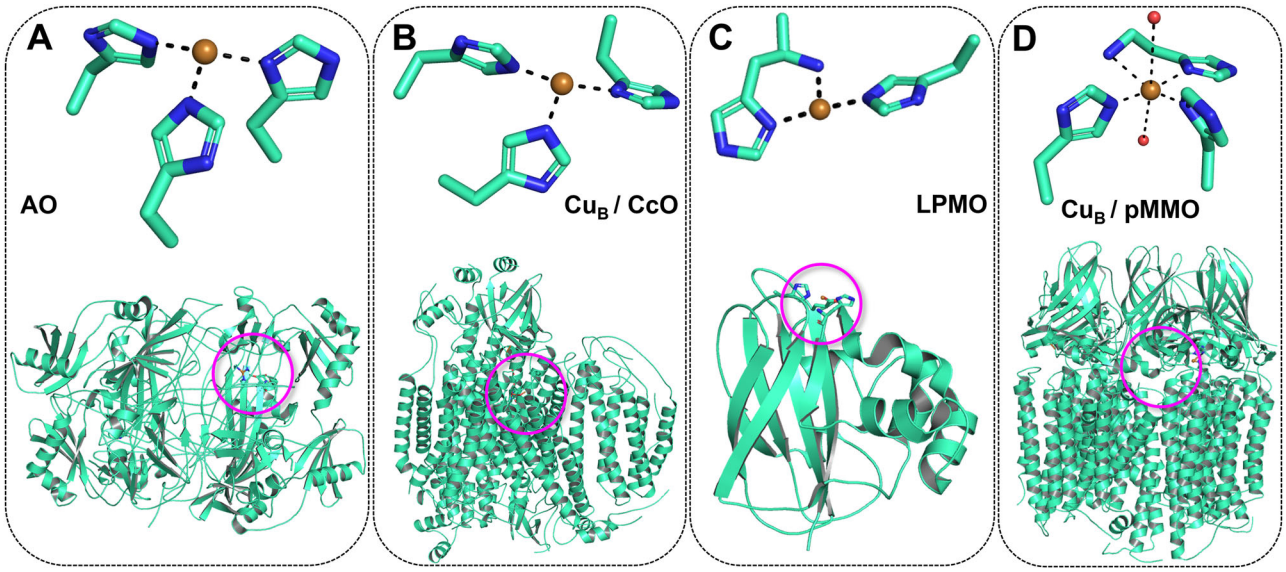

Fig. 1 | Select Cu proteins with CuN_3 or CuN_4 binding sites. A Amine oxidase (AO), PDB: 2W0Q, **B** the Cu_B site of cyt c oxidase (CcO), PDB: 2OCC, and **C** lytic polysaccharide monooxygenase (LPMO), PDB: 5FJQ feature three protein-derived nitrogen ligands. The Cu_B site of particulate methane monooxygenase (pMMO), PDB: 7S4H, has a $(His)_3(NH_2)$ ligation (**D**) with axial waters. The cartoons are shown in turquoise, His as turquoise/blue sticks, Cu as an orange sphere, and water as red spheres. The figure is made in PyMol.

hydrocarbon monooxygenase reduces the enzymatic activity by >80%[28]. Besides being unreactive to exogenous substrates, the Cu_B site is also difficult to reduce[25]. Thus, the Cu_B appears to be a structural site but is still important for function[25]. The unreactive nature of the Cu_B is intriguing, given that many synthetic Cu complexes with tripodal tetradentate ligands can activate O_2 and H_2O_2[29–32].

How the structural differences translate to function that makes a $Cu(His)_2NH_2$ site (LPMO, etc.) active to exogenous substrates but not the $Cu(His)_3NH_2$ site of pMMO Cu_B remains unknown. Given that the active sites are embedded in diverse protein matrices of varying secondary and tertiary structures, it becomes challenging to attain a unified and generalized view of how the coordination number, ligand environment, and remote interactions influence ET, λ, and H_2O_2/O_2 reactivity, ultimately determining functional outcomes. Governed by the primary sequence repeat pattern, the de novo protein design approach enables the creation of active sites within similar structural motifs, such as the α-helix, offering insights into how the immediate coordination environment of metalloenzymes determines their functions[3,33–35]. The knobs-into-holes (KIH) packing of hydrophobes provides a distinctive handle to produce self-assemblies[36–38] with controlled oligomeric states where an active site of interest can be introduced. Given the modular nature of the design, different types of coordination numbers and geometries can be constructed within de novo proteins, as dictated by self-assembly. Indeed, recent success has been achieved in creating artificial metalloenzymes (ArMs) within de-novo scaffolds [39–48].

One such example is the artificial Cu proteins (ArCuPs) that function as peroxidases and peroxygenases featuring $Cu(His)_3$ active sites within trimeric (3SCC) self-assemblies[45,46]. The 3SCC ArCuP activates H_2O_2[45] and electrocatalyzes the $2e^-$ and $4e^-$ oxidation and peroxygenation[44]. To elucidate what factors control the physical and reactivity outcomes of $Cu(His)_2NH_2$ vs. $Cu(His)_3NH_2$ sites in biology that make the former reactive but the latter unreactive, we have designed a $Cu(His)_4$ site within a de novo designed tetrameric ArCuP (4SCC), as a model of the pMMO Cu_B site. We demonstrate how the differences in the coordination properties of 4SCC and 3SCC alter their O_2 and H_2O_2 activation and ET properties. The reduction and reoxidation kinetics probed by electronic and EPR spectroscopy suggest that 3SCC is easier to reduce and reoxidize than 4SCC. The 4SCC is also unreactive to the peroxygenation of C-H substrates. To address how coordination differences influence ET properties and the resultant catalytic outcomes, the λ values of these ArCuPs have been experimentally determined. 4SCC has an inherently higher λ than 3SCC, which is significantly dominated by the solvent reorganization energy, mediated by an H-bond involving a primary-sphere His and a second-sphere Glu, which enables the formation of an extended H_2O-mediated H-bonding network. Intriguingly, when this H-bond is deleted, the water-mediated H-bonding network is also removed. This lowers the solvent reorganization and renders the inactive 4SCC to become an active peroxidation catalyst.

Results and discussion

Design of modular peptide assemblies

A hallmark of de novo protein design is the ability to construct self-assemblies with different oligomeric states by changing the primary sequence. This is achieved by controlling the KIH packing of *a* and *d* site residues in the heptad $(abcdefg)_n$. For example, introducing an Ile at the *a* and *d* site of the heptad $(IAAIKQE)_n$ produces the trimeric 3SCC ArCuP[45]. To design the tetrameric 4SCC assembly, the $(LAAIKQE)_n$ motif was chosen, having a Leu at the *a* site and an Ile at the *d* site[49]. A five-heptad sequence was chosen to optimize packing and ensure tetramer formation with the desired metal coordination number. To introduce the His site in 4SCC, we chose the 9th position of the heptad, similar to the 3SCC, to allow a direct assessment of how the immediate coordination environment alters their physical and reactivity properties. The Ala residues favor the α-helix formation, while the Glu and Lys at *e* and *g* positions control the parallel orientation of the helices by ion pairs. An acetylated and amidated Gly residue caps the N- and C- termini, respectively. A Trp chromophore is introduced at an *f* site on the last heptad to aid in quantification. The final sequence of 4SCC is shown in Table 1.

Structure and electronic properties of 4SCC

4SCC was crystallized in the Cu-bound form and diffracted to 1.36 Å (statistics in Table S1). The structure reveals that 4SCC has a tetrameric quarternary structure produced by parallel assembly of the monomers (Fig. 2A), as designed. All four His residues point toward the helical axis and bind Cu exclusively via the N_ε atoms. A water molecule occupies an

axial position at 2.6 Å, forming an approximate square pyramidal $Cu(His)_4OH_2$ coordination (Fig. 2B). The His residues are slightly distorted from the Cu plane with Cu-N_ε distances of 2.0–2.2 Å (Fig. 2C). In the Cu_B site of pMMO, the Cu-N_{His} distances range from 2.1–2.3 Å, and Cu-NH_2 distance is 2.5 Å[24]. Two opposing N_ε atoms in 4SCC are located below Cu with an $\angle N_\varepsilon$-Cu-N_ε angle of 167° (Fig. 2D). The remaining two N_ε atoms lie above the Cu with an $\angle N_\varepsilon$-Cu-N_ε angle of 189°. The $\angle N_\varepsilon$-Cu-N_δ and $\angle N_\delta$-Cu-NH_2 angles in the pMMO Cu_B site are 119° and 161°, respectively (Fig. S1). In 4SCC, the orientation of His C_ε atoms is such that two opposing His residues are tilted away from each other at a greater extent than the others (140° vs. 163°). The electronic spectrum of 4SCC has a d-d band (Fig. 2E) at ~600 nm. The EPR spectrum of 4SCC (Fig. 2F) is characteristic of a tetragonally elongated type-2 Cu center having an axial g tensor, with $g_{x,y} = 2.048$, $g_z = 2.253$ and resolved Cu hyperfine splittings of $A_{x,y} = 71$ MHz and $A_z = 543$ MHz (Table S2). Additional superhyperfine splittings from the ^{14}N nuclei of four His ligands are observed with $A_{N(x,y)} = 51, 41, 44, 41$ MHz, and $A_{N(z)} = 55, 41, 44, 41$ MHz. The observation of well-resolved Cu-^{14}N(His) superhyperfine splittings suggests a high degree of structural homogeneity in the Cu coordination sphere of 4SCC. Finally, the axial symmetry ($g_z > g_x = g_y$) indicates that the unpaired electron resides in the d_{x2-y2} orbital, pointing toward the four N ligands on the tetragonal plane.

Table 1 | Peptide sequences used in this study

Peptide	Sequence
3SCC	Ac-G-IAAIKQE-HAAIKQE-IAAIKQE-IAAIKWEG-$CONH_2$
A10W-3SCC	Ac-G-IAAIKQE-HWAIKQE-$(IAAIKQE)_2$-G-$CONH_2$
4SCC	Ac-G-LAAIKQE-HAAIKQE-$(LAAIKQE)_2$-LAAIKWE-G-$CONH_2$
A10W-4SCC	Ac-G-LAAIKQE-HWAIKQE-$(LAAIKQE)_3$-G-$CONH_2$
K6E/E8K-4SCC	Ac-G-LAAIEQK-HAAIKQE-$(LAAIKQE)_2$-LAAIKWE-G-$CONH_2$

Reactivity differences between 3SCC and 4SCC

3SCC catalyzes H_2O_2 reduction electrochemically[45]. However, 4SCC does not, as no significant catalytic current corresponding to H_2O_2 reduction is observed with the latter (Fig. S2). 3SCC also electrocatalyzes the oxidation and peroxygenation of benzylic C-H substrates with catalytic proficiencies ($1/k_{TS} = k_{cat}/K_M/k_{uncat}$) in the 300–1200 M^{-1} range. The catalytic proficiencies can be enhanced by outer-sphere steric modifications that affect catalysis by facilitating substrate access, influencing the nature of Cu-oxygen species, and improving stabilities[46]. On the contrary, 4SCC does not peroxygenate or oxidize these substrates. This is evidenced by the small catalytic current and charge (Fig. S3) and a lack of product after electrolysis. These results indicate that differences in metal coordination in our de novo ArCuPs are critical determinants of their reactivity. This is consistent with the fact that Cu active sites with three protein-derived N ligands (e.g., LPMO, AO, Cu_B of CcO, NiR, etc.) are reactive, while the Cu_B site of pMMO, which has four protein-derived ligands, is not.

3SCC is easier to reduce than 4SCC

The reactive Cu^I form is necessary for generating the Cu-oxygen intermediates[6,16]. Given the coordination differences between 3SCC and 4SCC, one would expect the inherent reducibility to be different, which could influence their reactivity. To test this, we assessed the reduction kinetics using Trp fluorescence as a reporter of the Cu oxidation state. In the original designs, a Trp was present at the end of the peptide, which is too far from the Cu site to show any oxidation-state-dependent emission change. Thus, the Trp was moved to the 10th position (A10W variants), one residue away from the Cu site (Fig. 3A–B). These constructs also produce the type-2 Cu sites (Fig. S4). Kinetics of $Cu^{II} \rightarrow Cu^I$ reduction with ascorbate (Asc) shows that A10W-3SCC is reduced faster than A10W-4SCC (Fig. 3C, S5, S6). The rates vary linearly with [Asc] (Fig. 3D), yielding second-order rate constants of 1.9×10^{-6} $M^{-1}s^{-1}$ and 7.6×10^{-8} $M^{-1}s^{-1}$ for A10W-3SCC and A10W-4SCC,

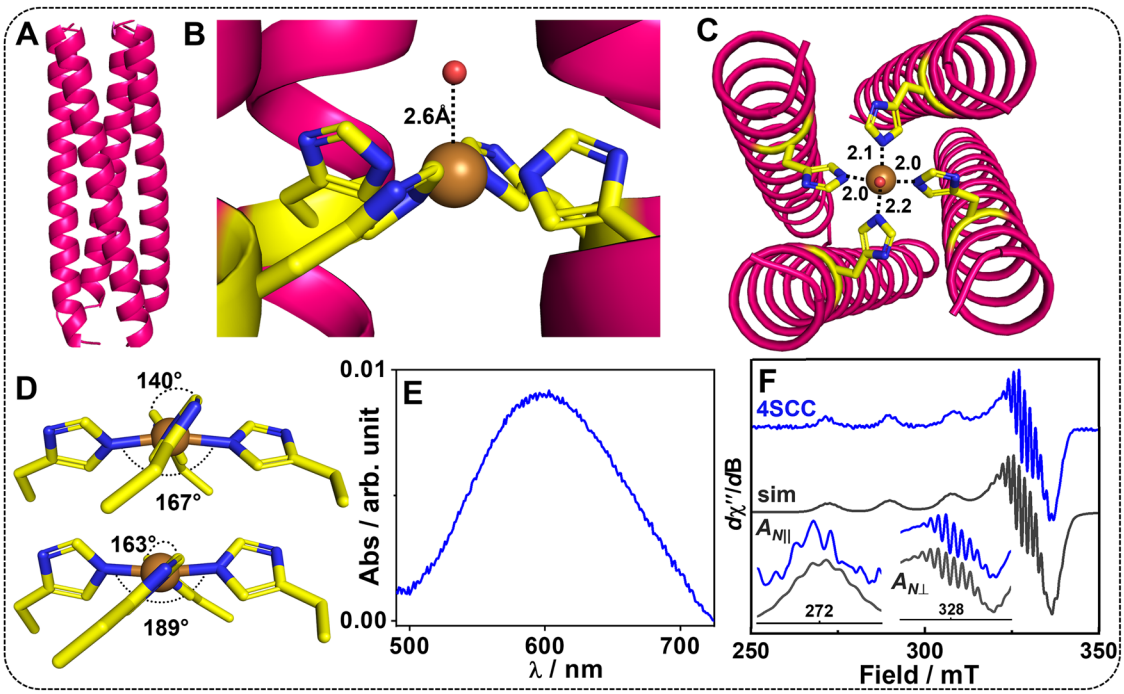

Fig. 2 | X-ray structure, UV-vis, and EPR analysis of 4SCC. A Cartoon representation of a 1.36 Å X-ray structure of 4SCC showing the parallel tetrameric assembly. **B** The square pyramidal Cu site, viewed perpendicular to the helical axis. **C** Views from the N-termini showing Cu binding to His N_ε atoms. **D** Orientations of the N_ε atoms relative to Cu. One set of N_ε-Cu-N_ε atoms from opposing His residues creates an obtuse angle, while the other set forms a reflex angle. The C_ε-Cu-C_ε orientations are wider in one set of His than in the other set. The axial water is omitted for clarity from **D**. The cartoons are shown in magenta, His as yellow/blue sticks, Cu as an orange sphere, and the axial water as a red sphere. Figures are generated in PyMol (PDB 8VHS). **E** d-d band of 4SCC. **F** The X-band EPR spectrum of 4SCC (blue) and the simulated spectrum (dark gray). Insets show expanded A_N splittings. EPR data was collected at 77 K.

https://doi.org/10.1038/s41467-025-57904-5

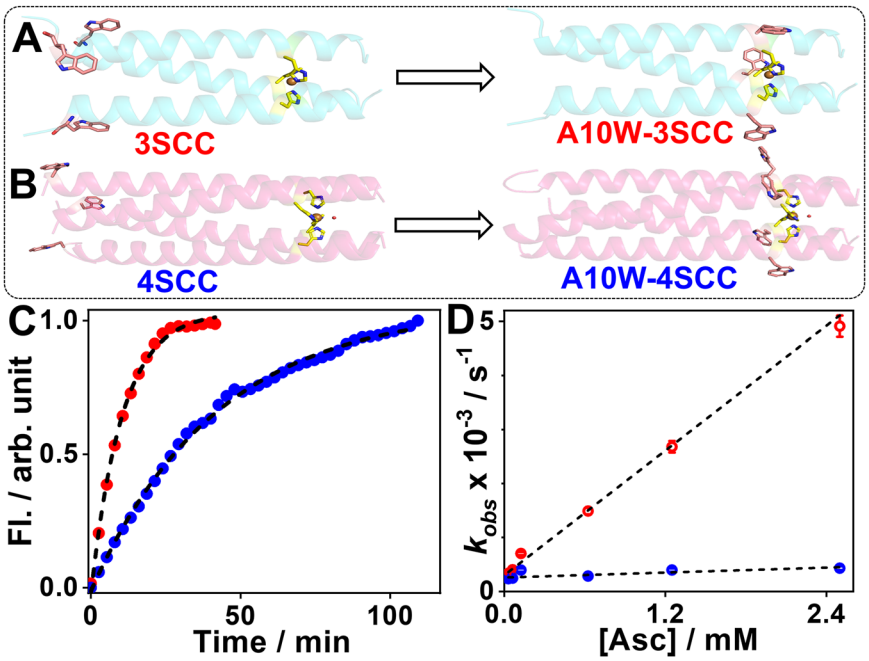

Fig. 3 | $Cu^{II\to I}$ reduction kinetics of A10W mutants monitored using Trp emission. Cartoon showing the A10W mutation in 3SCC (**A**) and 4SCC (**B**) to bring the Trp closer to Cu. **C** Reduction of Cu^{II}-A10W-3SCC (red) and Cu^{II}-A10W-4SCC (blue) by Asc. **D** The k_{obs} depend linearly on [Asc] with a significantly higher rate in 3SCC than in 4SCC. Here, 0.125 mM Cu^{II}-ArCuPs were anaerobically mixed with varying [Asc] in 10 mM MES buffer pH 6.5, and time-dependent emission was monitored (C shows the data with 10-fold Asc). The error bars in D represent SD from three independent measurements. λ_{ex} = 280 nm, λ_{em} = 340 nm for 3SCC and λ_{em} = 345 nm for 4SCC.

respectively (Table S3). The two orders of magnitude rate difference validate the notion that the Cu^{I} state is easily accommodated within a $Cu(His)_3$ motif rather than $Cu(His)_4$, a conclusion consistent with the experimentally determined λ of these ArCuPs (*vide infra*). In LPMO, the rate of reduction is fast and not rate-limiting[17]. In contrast, the Cu_B site of pMMO is reluctant to reduce[25]. Our results with 4SCC mirror this lack of reducibility of the pMMO Cu_B site.

H_2O_2 and O_2-dependent reoxidation

LPMOs can utilize either O_2 or H_2O_2 as an oxidant[16–21]. To establish the relative differences in H_2O_2 vs. O_2 activation, reoxidation studies of Cu^{I}-ArCuPs with each oxidant were performed. In both cases, the final species is in the Cu^{II} oxidation state (*vide infra* EPR). In contrast to Cu^{II}-3SCC, which produces the Cu^{II}-hydroperoxo species with H_2O_2[45], the Cu^{I} reactivity is more complex (Fig. 4A).

In the peroxide pathway of LPMO, the Cu^{I}--H_2O_2 association complex undergoes homolytic O-O bond cleavage to produce Cu^{II}-OH and ·OH by Fenton-type chemistry[17,21]. H-atom abstraction (HAA) by the ·OH produces the oxyl Cu^{II}-O· and H_2O. In the O_2-dependent pathway, cupric superoxo Cu^{II}-$O_2^{\bullet-}$ is produced initially, which, upon H^+/e^- transfer, is converted to Cu^{II}-OOH. The distal O protonation and ET produce the oxyl and H_2O. The corresponding proximal O protonation produces the Cu^{I}-H_2O_2 association complex, which enters the H_2O_2-dependent pathway. Thus, the reoxidation of Cu^{I}-LPMO with H_2O_2 can produce various Cu-oxygen species, such as Cu^{II}–OH---OH·, Cu^{II}–O·, or Cu^{II}–OH[17]. By analogy, we expect similar species to be produced during reoxidation of the ArCuPs.

When reacted with H_2O_2, Cu^{I}-3SCC produces a prominent band at ~332 nm (Fig. 4B). A definitive assignment of this species is challenging due to many possibilities, as discussed above. A Cu^{II}-hydroperoxo species appears in several model complexes in the 325-350 nm range[50–52]. Although Cu^{II}-OOH can be prepared with Cu^{II} and H_2O_2 or from Cu^{I} + O_2 in the presence of an electron and proton source, in one example, a Cu^{II}-hydroperoxo species has been produced from Cu^{I} and H_2O_2[53]. In this case, after the initial formation of Cu^{II}-OH and ·OH from the homolytic cleavage, the ·OH reacts with Cu^{I} to produce more Cu^{II}-OH, which then reacts with H_2O_2 to produce Cu^{II}-OOH and H_2O (Fig. S7). In the absence of substrate, when Cu^{I}-3SCC is reacted with H_2O_2, the active site His is oxidized[45], as observed in LPMOs as well[16,20]. The reaction product of Cu^{I}-3SCC and H_2O_2 is best assigned as a Cu^{II}-oxygen species with a partially oxidized His.

The reaction of Cu^{I}-3SCC with O_2 is ~11-fold slower than with H_2O_2 as monitored by UV-Vis (Fig. 4C, S8), producing a major band at ~336 nm plus a weaker feature at ~422 nm and another broad absorption around 540-570 nm. These features are typically observed for Cu-oxygen species, namely, Cu^{II}-hydroperoxo or Cu^{II}-alkylperoxo [54,55].

Cu^{I}-4SCC with both H_2O_2 and O_2 produces a similar species, with weak features at ~430 nm and 545 nm and a broad shoulder around 360 nm (Fig. 4D, E). 4SCC has poor reactivity, as no noticeable change in absorption features is observed at longer time points.

The reoxidation of Cu^{I}-3SCC-A10W with H_2O_2 and O_2 occurs at a rate comparable to that of Cu^{I}-3SCC, and it also peroxidizes benzyl alcohol (Fig. S8). The reoxidation was monitored by Trp quenching as well. Increasing the molar ratio of H_2O_2 (10 to 50-fold) quenched the Trp signal (Fig. 4F, G) for A10W-3SCC, with a second-order rate (k_{reox}) of 1.6×10^{-4} $M^{-1}s^{-1}$ (Table S3). At higher H_2O_2 concentrations, saturation is observed in A10W-4SCC (Fig. 4G) with a k_{reox} of 2.8×10^{-5} $M^{-1}s^{-1}$. Analogous experiments with O_2 saturated solutions show that Cu^{I}-A10W-3SCC reoxidation is faster than Cu^{I}-A10W-4SCC (Fig. S9), with a pseudo-first-order rate of 0.0019 s^{-1} for the former. No kinetic information was extracted for A10W-4SCC due to its poor reactivity with O_2.

Time-dependent EPR is further used to examine the reoxidation of Cu^{I}-ArCuPs with saturated O_2 solutions or with 100-fold excess H_2O_2 anaerobically. With O_2, a gradual reoxidation is observed (Fig. 5A, C), producing a major species (~ 70%) with $g_{x,y}$ of 2.059, g_z of 2.276, and A_z of 525 MHz (Table S2), and a minor species with g values of 2.054, 2.309, and A_z of 489 MHz. With H_2O_2, the signal saturates within ~30 min (Fig. 5B, C), further validating the faster reoxidation process than O_2. The major species (80%) produced with H_2O_2 have $g_{x,y}$ of 2.057 and g_z of 2.265, and A_z of 534 MHz (Table S2), while the remaining

https://doi.org/10.1038/s41467-025-57904-5

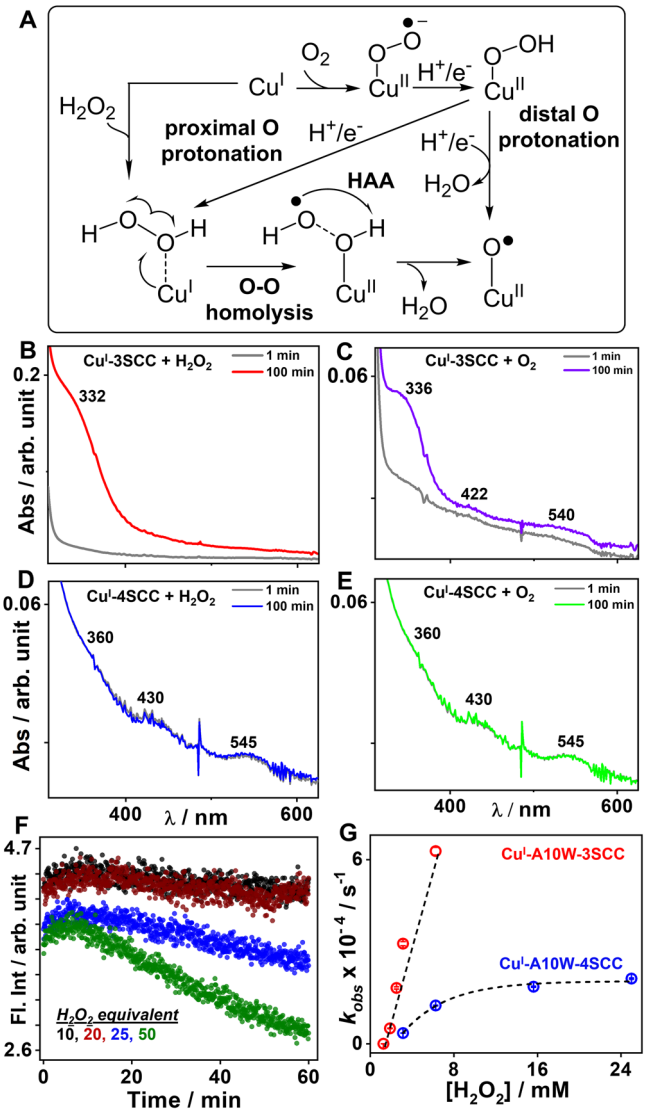

Fig. 4 | H_2O_2 and O_2 activation by the ArCuPs monitored by UV-vis and Trp emission. A H_2O_2 vs. O_2 activation pathways delineating the production of various Cu^{II}-oxygen species. **B**–**E** Reoxidation of 3SCC and 4SCC with H_2O_2 and O_2 monitored by UV-vis. The time traces represent spectra collected at 1 min (gray) and 100 min (red, violet, blue, green) after initiating the reactions. **F** The H_2O_2-dependent (black = 10, wine = 20, blue = 25, and green = 50-fold) reoxidation of A10W-3SCC monitored by Trp emission, and **G** the k_{obs} vs. [H_2O_2] plots for A10W-3SCC (red), and A10W-4SCC (blue). Error bars in **G** represent SD from three experiments. [ArCuP] = 0.125 mM, pH = 6.5. For oxygenic reoxidation, O_2-saturated solutions were used.

20% of the species have g values of 2.063, 2.299, and A_z of 489 MHz. The reoxidation is much slower for the CuN_4 site (Fig. S10, S11), as anticipated.

To summarize, 3SCC undergoes faster reoxidation, having higher rates with H_2O_2 than O_2, like LPMOs[16]. The low reactivity of 4SCC resonates with the inertness of the Cu_B site of pMMO [25].

Redox properties of the ArCuPs

Protein-film voltammetry was used to determine the redox properties of the ArCuPs adsorbed on a pyrolytic graphite electrode (PGE). Repeated cyclic voltammetry (CV) scans show that the ArCuPs remain stable on the electrode surface (Fig. S12)[45]. The cathodic and anodic peak currents vary linearly with the scan rate, suggesting a surface-controlled redox process. Both the ArCuPs have E°′ in a narrow range, with a difference of −16 mV, 256 mV for 3SCC[45], and 240 mV for 4SCC (Fig. 6A) at pH 6.5. These E°′s are similar to the range of other His-coordinated type-2 Cu proteins irrespective of their role as catalytic or ET sites[1,6]. The CV for 4SCC is broader than 3SCC, which suggests a slower ET and that dispersion effects contribute to the redox process [56].

4SCC has a higher λ than 3SCC, with a significant solvent contribution that is negligible in 3SCC

We have probed the ET properties to investigate how factors beyond the primary coordination influence the reactivity differences between the ArCuPs.

As the Marcus Eq. (i) describes, ET depends on λ [57,58].

$$k_{ET} = \frac{4\Pi^2 H_{AB}^2}{h\sqrt{4\Pi\lambda k_B T}} \exp\left[-\left(\Delta G^0 + \lambda\right)^2 / 4\lambda k_B T\right] \quad \text{(i)}$$

The total λ (λ_T) for metalloproteins is contributed by the inner-sphere (λ_{Cu}) and the outer-sphere (λ_{OS}) reorganization, which comprises the surrounding protein matrix (λ_P) and the solvent (λ_{H2O}) reorganization[4,59,60]. The λ_{Cu} reports any geometrical changes associated with the redox event at the Cu site. Traditionally, λ for Cu proteins such as azurin (Az) has been determined by photoexcitation followed by flash-quench of Ru/Os modified Az[60] or pulse radiolysis[61]. Electrochemistry is an alternative method to derive λ from Arrhenius's analysis of temperature-dependent ET rates[62–65]. We have employed two electrochemical methods to determine λ: rotating disk electrochemistry (RDE) and chronoamperometry (CA). In RDE, the ArCuPs are dissolved in solution, and linear sweep voltammograms (LSVs) at different electrode rotation rates are measured as they diffuse to the electrode surface (Fig. 6B, S13–S16). Since the protein is in solution, λ measured from RDE has both the inner-sphere (λ_{Cu}) and outer-sphere components ($\lambda_P + \lambda_{H2O}$). The ET rates ($k_{ET}$) thus determined (see Methods for details) are subjected to Arrhenius analysis (Fig. 6C) to obtain λ_T. The λ_T obtained using this method is 0.34 eV for 3SCC and 0.89 eV for 4SCC (Fig. 6D, Table 2).

Contrary to the RDE method, the λ measured by CA are obtained from ArCuPs that are directly immobilized on the electrode surface. Therefore, contributions from the solvent reorganization are expected to be minimal compared to situations where the protein is freely diffusing in solution[62,63]. Thus, the λ determined using CA has contributions from the Cu site and any changes to the polypeptide matrix during ET. We denote this sum as $\lambda_{Cu\text{-}P}$. Naturally, the difference in λ_T measured by RDE and $\lambda_{Cu\text{-}P}$ measured from CA will yield the solvent contribution, λ_{H2O} ($\lambda_{H2O} = \lambda_T - \lambda_{Cu\text{-}P}$). From this analysis (Fig. 6E, S17–S22), the average $\lambda_{Cu\text{-}P}$ of 0.36 eV is obtained for 4SCC and 0.27 eV for 3SCC (Fig. 6F, Table 2), which yields λ_{H2O} of 0.07 eV for 3SCC and 0.53 eV for 4SCC. These results imply that not only does the 4SCC have a higher λ_T than 3SCC, but a significant solvent contribution, λ_{H2O} of 0.53 eV, is present in 4SCC but not in 3SCC.

λ comparison between ArCuPs and Cu proteins

In classical Cu complexes, λ is high, ~1.88-2.4 eV[66]. However, the protein fold significantly lowers λ, as seen in various type-1 Cu sites (Table 2)[60,67–73]. A flexible coordination produces a higher λ than a constrained site in Az mutants, as exemplified by C112D-Az (type-2) or C112D/M121L-Az (type-0) Cu sites[74,75]. An exception is Cu-Aβ16, which has a low λ of 0.3 eV[76], similar to 3SCC, despite being unstructured. The low λ has been ascribed to a preorganized ET process that minimizes structural changes. In select cases of synthetic Cu complexes, λ is ~0.95[77] – 1.1 eV[78], with λ_{Cu} of 0.4 eV in one example[78], comparable to 4SCC.

https://doi.org/10.1038/s41467-025-57904-5

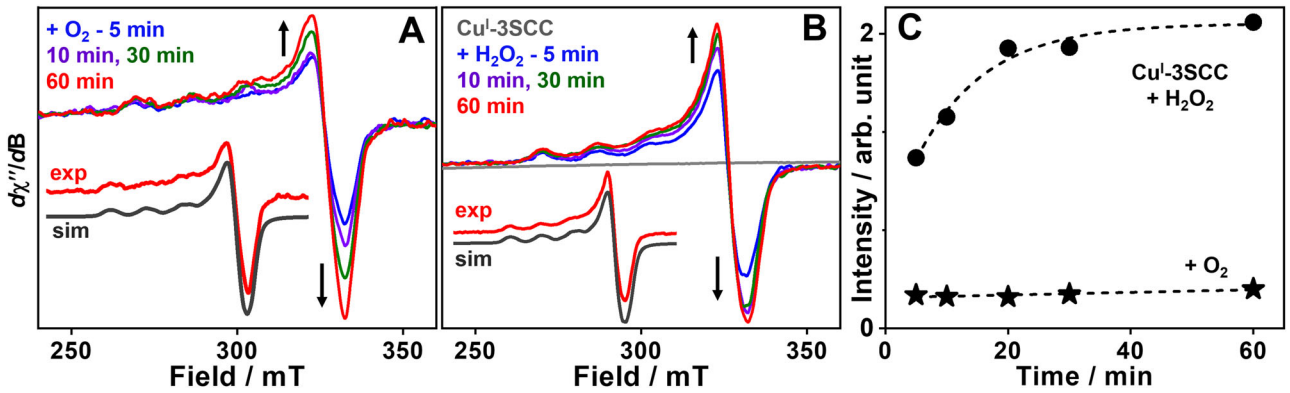

Fig. 5 | H_2O_2 and O_2-dependent reoxidation of Cu^I-3SCC monitored by EPR. Time-dependent X-band EPR data for the reoxidation of 3SCC with O_2 (**A**) and H_2O_2 (**B**) at 5 min (blue), 10 min (violet), 30 min (green), and 60 min (red). Cu^I-3SCC in B is shown as a gray trace. **C** The corresponding EPR intensity plot vs. time from double integrations (H_2O_2 = circles; O_2 = stars). A 100-fold H_2O_2 was used in these experiments, and samples were frozen at various intervals. For O_2, Cu^I-peptide was mixed with an equal volume of O_2-saturated buffer, stirred, and then frozen at different intervals. The simulated spectra for 60-min samples are shown as insets in A and B. Final [ArCuP] = 0.5 mM. Data were collected at 77 K. pH = 6.5.

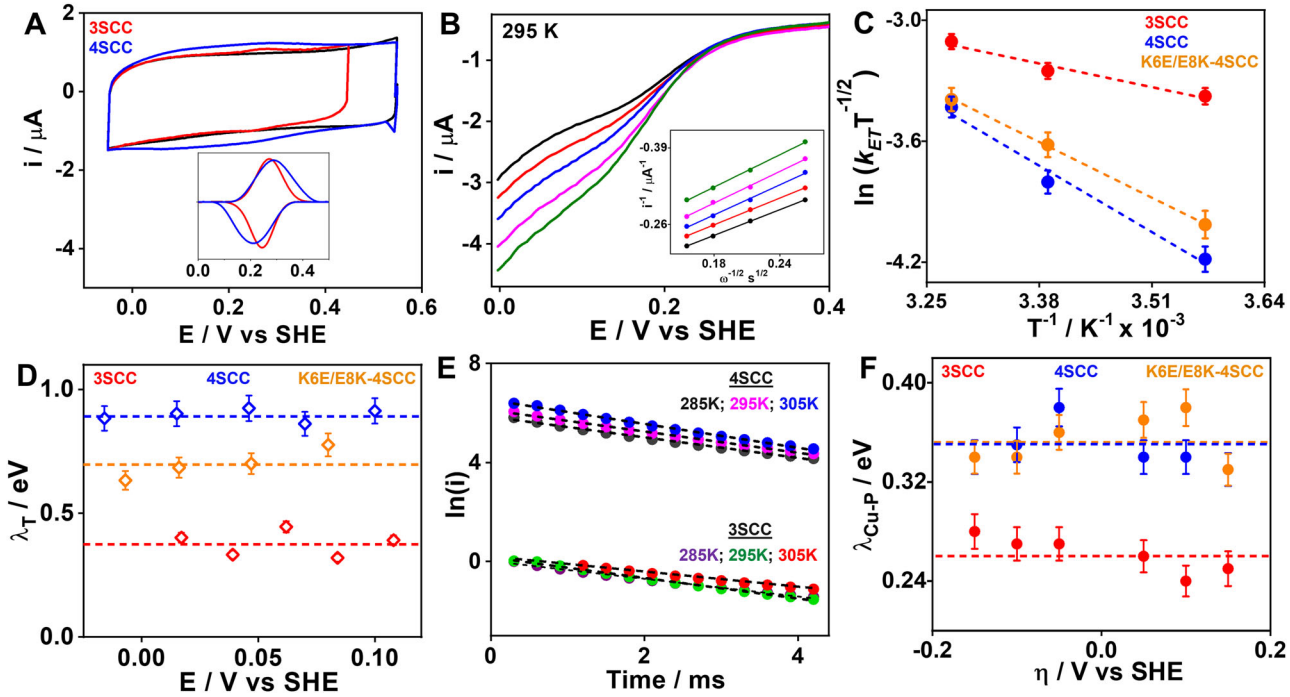

Fig. 6 | Experimental determination of reorganization energies of the ArCuPs using electrochemistry. A CVs for 3SCC (red), 4SCC (blue), and the blank electrode (black) in 80 mM mixed buffer pH 6.5. Scan rate = 50 mV/s. The inset shows background corrected redox peaks. **B** RDE data for 0.25 mM 3SCC solutions at 295 K in 80 mM mixed buffer, 100 mM KCl at pH 6.5. Rotation rates = 250 rpm (black), 512 rpm (red), 850 rpm (blue), 1300 rpm (magenta), and 1850 rpm (olive). The inset shows the Koutecký-Levich (K-L) plots in the mass transport region used to obtain k_{ET}. The data are shown at potentials 0.017 V (black), 0.039 V (red), 0.062 V (blue), 0.084 V (magenta), and 0.108 V (olive). **C** Arrhenius plots were constructed using the k_{ET} obtained from the K-L analysis. **D** λ_T at different potentials obtained from the slopes of the Arrhenius plots. The dashed lines show the average λ_T. **E** *ln(i) vs. t* plots obtained from CA experiments. The slopes yield k_{app} (s^{-1}) at a fixed η (data shown for η = 100 mV; see the SI for the remaining). **F** $\lambda_{Cu\text{-}P}$ measured from CA experiments at different η values. The dashed lines show the average $\lambda_{Cu\text{-}P}$. The error bars represent SD from 2-3 independent sets of experiments. For CA experiments, 10 μL of 0.25 mM ArCuPs were dropped on PGE and dried under N_2, and data were collected in 80 mM mixed buffer at pH 6.5. In **C**, **D**, and **F**, 3SCC is red, 4SCC is blue, and K6E/E8K-4SCC is orange.

Correlating structural differences to ET and catalysis

A less saturated $Cu(His)_3$ coordination of 3SCC is expected to lower $\lambda_{Cu\text{-}P}$ than a more saturated 4SCC, which is observed here. However, to rationalize the presence of a significant solvent reorganization in 4SCC, one must look beyond the primary-sphere. Indeed, differences exist between the second and outer coordination-sphere interactions. Specifically, the His9 residues in 4SCC participate in second-sphere H-bonding with Glu8 from a neighboring helix via the available N_δ atoms (Fig. 7A). No such interaction is observed in 3SCC (Fig. 7B), even though both peptides have the -GluHis- motif in their heptads. Twelve H_2O molecules constitute an extended outer-sphere H-bonding network in 4SCC involving Glu8 (Fig. 7A). These structural differences alter the physical properties of the ArCuPs, which are translated to their function.

First, the second-sphere H-bonding will increase the electron density on the imidazole ring, making the Cu^{II} state more stable than the Cu^I state. Second, as seen here, the extended H_2O-mediated H-bonding network will increase the outer-sphere contribution to λ_T.

https://doi.org/10.1038/s41467-025-57904-5

Table 2 | Selected λ for Cu proteins and model complexes

Example	λ / eV	Ref
Az	0.82	ref. 60,68.
Plastocyanin	0.70–0.75	ref. 69.
Az variants	0.67–0.98	ref. 70,71.
Cu_A-Az	0.4	ref. 72.
AxCuNiR AcCuNiR	0.77 0.57	ref. 73.
blue AxCuNiR (T2)	1.6	ref. 94.
C112D-Az C112D/M121L-Az	2.1–2.3 0.9-1.1	ref. 74,75.
Aβ16	0.3	ref. 76.
3SCC	$\lambda_T = 0.34$; $\lambda_{Cu\text{-}P} = 0.27$; $\lambda_{H2O} = 0.07$	this work
4SCC	$\lambda_T = 0.89$; $\lambda_{Cu\text{-}P} = 0.36$; $\lambda_{H2O} = 0.53$	
K6E/E8K-4SCC	$\lambda_T = 0.69$; $\lambda_{Cu\text{-}P} = 0.36$; $\lambda_{H2O} = 0.33$	
3SCC-($O_2/O_2^{\bullet-}$)	1.12	
4SCC-($O_2/O_2^{\bullet-}$)	1.39	
$[LCu^{III/II}OH]^{0/-}$	0.95	ref. 77.
$[Cu_2^{II}(UN\text{-}O^-)(O_2^{\bullet-}/O_2^{2-})]^{2+/+}$	1.1 (λ_{Cu} = 0.4 eV)	ref. 78.
$[Cu^{II/I}(phen)_2]^{2+/+}$ $[Cu^{II/I}(bpy)_2]^{2+/+}$	2.40 1.88	ref. 66.

Therefore, the combined primary, secondary, and outer-sphere H-bonding involving H_2O molecules add to the higher λ_T in 4SCC, with the major contribution coming from the solvent reorganization. This observation is coherent with the hybrid quantum mechanics/molecular mechanics (QM/MM) simulation on Az, where the solvent reorganization around His117 is proposed to contribute ~80% of the total λ[79]. The coordination environment of 3SCC and the absence of second-sphere and outer-sphere water-mediated H-bond lowers λ_T, with nearly all the contribution coming from the active site alone. In 3SCC, a single Glu8-H_2O H-bond is present (PDB 7L33), but since Glu8 does not make an H-bond with primary-sphere ligand His9, the effect of outer-sphere solvent reorganization is expected to be negligible, as seen here. The slower reaction kinetics of 4SCC with O_2 or H_2O_2 and its lack of reactivity for C-H oxidation can be attributed to a significant solvent reorganization barrier compared to 3SCC.

One possible factor for the unreactivity of the pMMO Cu_B site, even to polar solutes such as nitrite, could be its high reorganization energy. Interestingly, several second-sphere and outer-sphere H-bonds involving amino acid residues and solvent molecules are present around the Cu_B site (Fig. 7D)[27]. Although λ determination for the Cu_B site will be nearly impossible, given the presence of multiple mononuclear Cu sites in pMMO, these extended outer-sphere interactions are expected to increase the reorganization energy barrier for this site, as we see in 4SCC.

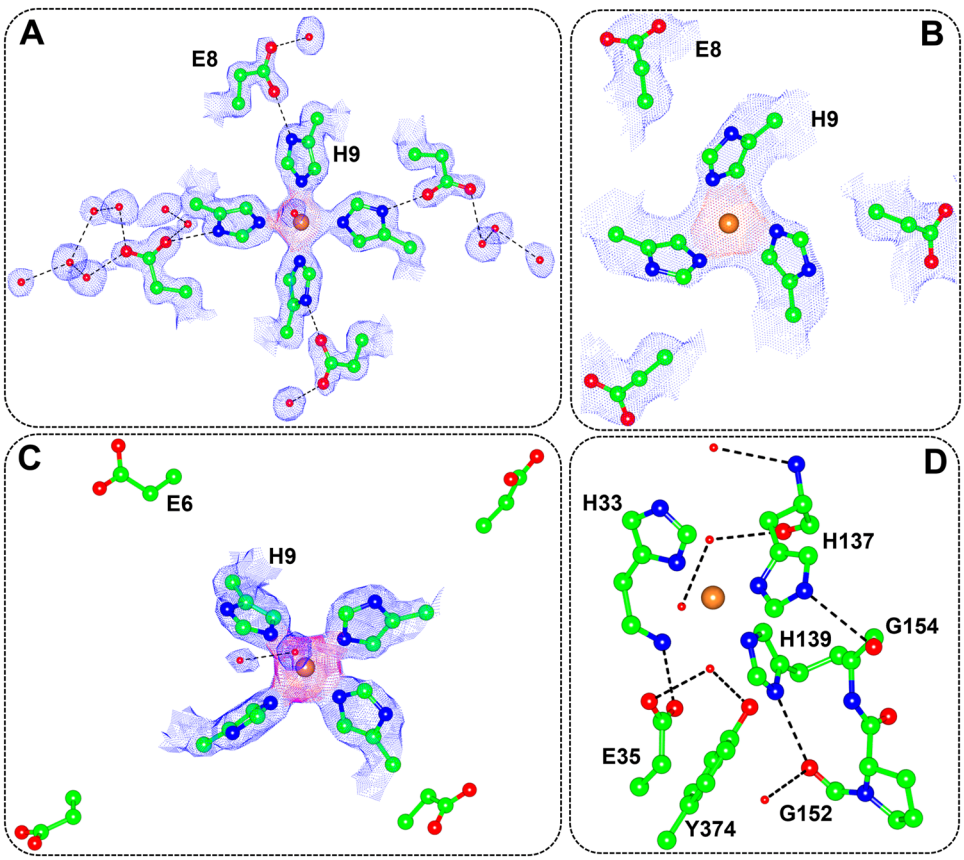

Fig. 7 | Structural analyses of the ArCuPs and pMMO Cu_B site showing the Cu site, 2nd-sphere, and outer-sphere interactions. X-ray structures of 4SCC (**A**: PDB - 8VHS) and 3SCC (**B**: PDB - 7L33) show that in 4SCC, the non-coordinating N_δ atoms of His9 make second-sphere H-bond with Glu8 from a neighboring helix, which is involved in extended H_2O-mediated H-bonding. The corresponding His residues in 3SCC do not make this H-bond despite having the EH sequence in the heptad. **C** X-ray structure of K6E/E8K-4SCC (PDB - 9BQR) shows that when Lys and Glu at the 6th and 8th positions are interchanged in the first heptad, the second-sphere H-bond between the His9 and Glu6 plus the H_2O-mediated H-bonds are no longer present, which lowers the λ_{H2O}. **D** The Cu_B site of pMMO (PDB - 7S4H) and its surrounding environment, showing the H-bonding network involving amino acids and solvent, are present. Figures are generated in CCP4mg. The Cu is shown as an orange sphere, and its electron density in **A**–**C** is drawn as a red mesh, with the remaining atom density being blue. In these ball-and-stick representations, carbon is green, oxygen is red, and nitrogen is blue. Waters are shown as small red spheres.

The poor reactivity of $Cu(His)_3NH_2$ or $Cu(His)_4$ sites in a protein or polypeptide framework is intriguing, as several synthetic CuN_4 complexes with tripodal tetradentate ligands activate O_2, H_2O_2, and C-H bonds[29–32]. One crucial factor governing this difference in reactivity is likely higher outer-sphere reorganization energy in biomolecular systems than in synthetic systems, which lack ligand and solvent-mediated extended H-bonding networks.

Deleting H-bonding interactions modulates λ_{H2O} and enables C-H oxidation

An important question in metalloprotein design is, "Is it possible to selectively alter reorganization energy by changing second- and outer-sphere H-bonding but keeping the primary coordination intact?" To address this, we designed a mutant to delete the Glu-His H-bond of 4SCC by replacing the Glu8 (*g* site heptad) with Lys. Consequently, the Lys6 (*e* site heptad) was changed to Glu to maintain the charge neutrality and *e-g* ion pairs. The $E^{o\prime}$ for the mutant (Fig. S23) is similar to 4SCC and other type-2 Cu sites. From RDE and CA (Fig. S24–26), the λ_T and $\lambda_{Cu\text{-}P}$ determined for K6E/E8K-4SCC are 0.69 eV and 0.36 eV, respectively (Fig. 6D, F; Table 2). This result shows that although the $\lambda_{Cu\text{-}P}$ is identical to the parent 4SCC, the λ_{H2O} is significantly reduced to 0.33 eV compared to 0.53 eV in 4SCC.

To investigate if the experimental λ values correlate to structure, we determined the X-ray structure of the double mutant (Fig. 7C). The Cu site is nearly identical to 4SCC (Fig. S27), although some disorder in the N-terminal region of chain D is present in the mutant. The EPR spectrum of the mutant lacks the Cu-^{14}N(His) superhyperfine splittings in both the perpendicular and parallel regions (Fig. S28) due to more flexibility caused by the deletion of the H-bond, agreeing with this disorder of Chain D. The relative orientations of the His residues are slightly different than 4SCC, causing minor variations in the $\angle N_\varepsilon$-Cu-N_ε and His C_ε angles (Fig. S1). As designed, the second-sphere His-Glu H-bond is eliminated. This, in turn, has removed the H_2O-mediated outer-sphere H-bonds involving the Glu residue as it is now 3-residue away from the His. The only H_2O-mediated H-bond is seen between the axial Cu-bound H_2O and a second H_2O nearby (Fig. 7C). Since the Cu site in 4SCC is located within the hydrophobic core, the deletion of second-sphere H-bonding does not alter the $Cu(His)_4$ site, leading to a similar $\lambda_{Cu\text{-}P}$ for both 4SCC and the mutant. However, deletion of the second-sphere H-bond removes the outer-sphere H_2O-mediated H-bonding besides the axial H_2O···H_2O H-bond, leading to a 0.2 eV lower λ_{H2O} in the mutant than 4SCC. The axial H_2O-mediated H-bond also contributes to a higher λ_{H2O} in the mutant than in 3SCC, which lacks any H_2O-mediated H-bond. These findings demonstrate that protein design makes it possible to modulate λ_{H2O} via selective modification of second- and outer-sphere H-bonding.

The absorption features of the mutant produced with H_2O_2 and O_2 (Fig. S28) are more pronounced than 4SCC, suggesting a more reactive nature of the former. In addition, there are also differences in band positions in the mutant, attesting to their reactivity differences. Next, we probed whether deleting the extended hydrogen-bonding interactions would make the double mutant active toward C-H oxidation. Unlike 4SCC, K6E/E8K-4SCC produces a significant catalytic current for benzyl alcohol peroxidation (Fig. S3) with H_2O_2. As a result, an appreciable amount of charge is observed in the controlled potential electrolysis (CPE) experiment, leading to the detection of benzaldehyde in the GC (Fig. 8). The k_{cat}, K_M, and k_{uncat} for K6E/E8K-4SCC were determined to be 1.31 s^{-1}, 37.3 mM, and 0.07 s^{-1}, respectively, producing a catalytic proficiency of 500 M^{-1}. This value is still lower than that of 3SCC (1200 M^{-1}), suggesting that differences in the primary coordination sphere remain a major contributor to activity. However, with the same CuN_4 primary coordination, K6E/E8K-4SCC is catalytically active, while 4SCC is not. We attribute this to a high solvent barrier caused by the extended H-bonding network of water molecules around the protein, mediated by the His−Glu H-bond. When this H-bond is removed in K6E/E8K-4SCC, the surrounding water-mediated H-bonding network is disrupted, lowering its λ_{H2O} and restoring its peroxidation activity.

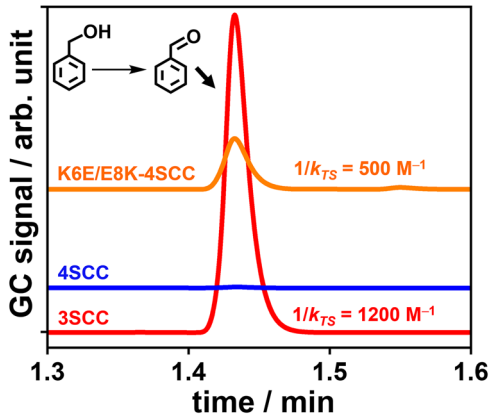

Fig. 8 | Benzyl alcohol to benzaldehyde peroxidation reactivity of the ArCuPs. GC traces for benzyl alcohol oxidation to benzaldehyde after 1 h of CPE experiment. Benzaldehyde was observed with 3SCC (red trace) and in the double mutant K6E/E8K-4SCC (orange trace), but no quantifiable product was observed with 4SCC (blue trace). After CPE, the product was extracted in DCM, dried over Na_2SO_4, and analyzed by GC.

These results demonstrate that protein design allows for controlled tuning of outer-sphere solvent reorganization energies while maintaining the primary coordination and enables switching on or off the activity of a metalloprotein by modulating H-bonding interactions.

In summary, an Ile/Ile to Leu/Ile switch of the hydrophobic layers enables the modulation of the oligomerization behavior in designing the ArCuPs, and structural and spectroscopic evidence supports the design. The 3SCC is easier to reduce and reoxidize than the 4SCC. Additionally, the 3SCC activates peroxide and oxidizes/peroxygenates C-H substrates, whereas the 4SCC does not. These chemical properties of 4SCC resemble the unreactivity of the pMMO Cu_B site. Cu^I-3SCC is more rapidly reoxidized with H_2O_2 than with O_2, similar to the peroxygenase reactivity of LPMOs in the absence of a substrate. The reaction profile of H_2O_2 and Cu^I-3SCC is complex, starting with homolytic O-O bond cleavage, leading to the Cu^{II}-oxygen species. Conversely, the O_2 reaction produces features consistent with a Cu-hydroperoxo species via an outer-sphere ET process.

The reactivity differences between 3SCC and 4SCC can be explained by inner-sphere and outer-sphere reorganization energies coupled with structural differences. A less-coordinatively saturated 3SCC accounts for its lower $\lambda_{Cu\text{-}P}$ than 4SCC. However, 4SCC has a significantly higher solvent contribution due to an extended H_2O-mediated H-bond network around the second-sphere Glu8, which is H-bonded to the primary-sphere His. These interactions increase the structural rigidity of 4SCC, leading to high reorganization energy and making it less reactive than 3SCC. Removing the second-sphere His9-Glu8 H-bond eliminates the extended H_2O-mediated H-bonding network, reducing the outer-sphere solvent contribution to the reorganization energy while maintaining the primary coordination. Consequently, the lower solvent reorganization barrier converts an inactive metalloprotein 4SCC into an active peroxidation catalyst. This activity switching by protein design to control outer-sphere solvent rearrangement is an exciting discovery. Our findings offer a new dimension to modulating the function, which we believe will be broadly applicable in metalloenzyme design.

Methods

General

All chemicals and reagents were used as received. Buffers were prepared in Milli-Q (Millipore) water, treated with Chelex-100 overnight, pH adjusted as necessary, and filtered. Tris(hydroxymethyl) aminomethane (Tris), 4-(2-hydroxyethyl)-1-piperazineethanesulfonic acid (HEPES), 2-(N-morpholino) ethanesulfonic acid (MES), sodium acetate, NaCl, and HCl were purchased from Fisher Scientific. The mixed buffers contained 20 mM each of MES, sodium acetate, HEPES, and Tris at the desired pH. $CuCl_2$ (Alfa Aesar), NaOH (VWR), and H_2O_2 (VWR) stock solutions were made in water, and ascorbic acid (VWR) stock was made in the buffer.

Peptide synthesis and purification

Peptides were synthesized at 0.25 mmol scale on a solid phase peptide synthesizer (CEM) using standard Fmoc chemistry with acetylated N-terminal and amidated C-terminal[45]. Cleavage from the resin and side chain deprotection was performed using the cocktail consisting of 92.5% trifluoroacetic acid (TFA: Advanced Chemtech), 0.25% triisopropylsilane (Sigma), 0.25% ethanedithiol (Sigma–Aldrich), and 0.25% water for 2 h. After filtration, TFA was evaporated, and peptides were precipitated using cold ether. Purification was done by reverse-phase HPLC (1260 Infinity II, Agilent) using a C_{18} semiprep column with water and acetonitrile solvent system supplemented with 0.1% TFA. Peptide mass was confirmed by MALDI mass spectrometry using the sinapinic acid matrix (Sigma).

X-ray crystallography

Solutions for Cu^{II}-4SCC were prepared by adding one equiv of $CuCl_2$ to 45 mg/mL apo peptide in basic water. K6E/E8K-4SCC was dissolved at 35 mg/mL in 20 mM Tris pH 8.5, followed by metallation. Crystals were grown using the hanging drop method at ambient temperature. Two µL of Cu^{II}-4SCC solution was mixed with an equal volume of the well solution containing 0.1 M Tris pH 8.5 and 2 M ammonium sulfate. For Cu^{II}-K6E/E8K-4SCC, two µL of this solution were mixed with two µL of the well solution containing 0.1 M Tris pH 8.5, 0.2 M $MgCl_2.6H_2O$, and 28% PEG 4000. The well volume was 1 mL. Crystals appeared within 7-20 days. The crystals were harvested and soaked with 30% PEG 400 as a cryoprotectant before flash-freezing in liquid N_2.

X-ray diffraction data were collected at the Life Sciences Collaborative Access Team (LS-CAT) of the Argonne National Laboratory, the Stanford Synchrotron Radiation Lightsource, and the FMX beamline at NSLS-II. Diffraction images were indexed and integrated in XDS[80], and scaled in Aimless[81]. Data quality assessment and twinning analysis were performed in phenix.xtriage[82]. The 4SCC structure was solved using Phaser[83] in CCP4i[84] by molecular replacement using 3R4A[85] as the search model, followed by automatic model building in Buccaneer[86]. Refinement was performed using phenix.refine[87] with iterative model building and density fitting analysis in Coot[88]. The K6E/E8K-4SCC was solved similarly, using 4SCC as the search model, and refined in Refmac5[89]. Structure validation was performed using the wwPDB OneDep System. The structure factors and coordinate files have been deposited with PDB code 8VHS for 4SCC and 9BQR for K6E/E8K-4SCC. Data collection statistics are in Table S1. 2mFo-DFc and mFo-DFc maps are in Fig. S29–30. Electron density maps shown in Fig. 7 were drawn in CCP4mg [90].

UV-vis spectroscopy

The spectra were recorded on an Agilent 8454 or Cary 5000 spectrophotometer. All samples were prepared in 10 mM MES buffer at pH 6.5. All solutions were degassed individually before mixing and starting the experiments. For the kinetics experiments, 0.125 mM ArCuP solutions and 12.5 mM H_2O_2 were mixed in a septa-capped anaerobic cuvette (Starna Cells) followed by monitoring the kinetics for 120 min with 1 min intervals in-between scans. Cu^{I}-peptides were prepared by adding one equivalent of Asc inside a glove box (MBraun) and incubating for 15 min. UV-vis was checked to ensure complete reduction. For kinetics with O_2, 0.25 mM Cu-peptides were mixed with an equal volume of an O_2-saturated buffer, and the kinetics started immediately. An O_2-filled balloon was used to maintain an O_2-saturated environment. Initial rates were calculated from the first 3 min of the kinetic run.

Fluorescence spectroscopy

Kinetics of Cu^{II} reduction with Asc and Cu^{I} reoxidation experiments with H_2O_2 were performed anaerobically by monitoring the Trp emission of A10W variants at pH 6.5 (10 mM MES) in septa-capped fluorescence cuvettes using a PTI fluorimeter. For reduction, 0.125 mM Cu^{II}-peptides were mixed with different equiv of Asc followed by continuous spectral monitoring. Reoxidation experiments were performed with 0.125 mM Cu^{I}-peptides (prepared by adding one equiv Asc to Cu^{II}-peptides) and an increasing concentration of H_2O_2. Each run was monitored for 120–180 min or until saturation was obtained, which depended on H_2O_2 concentration. In these experiments, the Trp excitation wavelength of 280 nm was used. An emission wavelength of 340 nm for A10W-3SCC and 345 nm for A10W-4SCC was selected based on the highest emission intensity. The final sample volume in each experiment was 800 µL.

Analysis of reduction and reoxidation kinetics

For reduction kinetics, the normalized fluorescence vs. time plots were fitted with a single-exponential function to extract the first-order rate constants at varying Asc concentrations. These rate constants were plotted against Asc concentration and fitted to a linear equation. The slopes of the linear fits represent the second-order rate constants with respect to Asc. A similar procedure was used for the reoxidation kinetics, except that the second-order rate constants were derived against varying H_2O_2 concentrations. This analysis was not performed for O_2 because, in O_2-saturated solutions, the O_2 concentration was assumed to be constant.

EPR spectroscopy

EPR data were collected at 77 K on a Bruker X-band (9.4168 GHz) EMXPlus Continuous Wave spectrometer at the School of Chemical Sciences EPR lab at the University of Illinois. Samples for EPR contained 0.5 mM ArCuPs in 100 mM MES pH 6.5 plus 25% glycerol as a glassing agent. A power of 10.02 mW was used with an attenuation of 13 dB, receiver gain of 30 dB, a modulation amplitude of 10 G, and a modulation frequency of 100 kHz. All instrument parameters were kept constant for each set of experiments. For reoxidation, a 100-fold H_2O_2 was added, and at different time intervals, samples were aliquoted to glycerol-containing EPR tubes and flash-frozen in liquid N_2 outside the glove box. For reoxidation experiments with O_2, one mM Cu^{I}-peptides was mixed with an equal volume of O_2-saturated buffer, and the reaction was allowed to proceed under an O_2 atmosphere outside the box with stirring. At different time intervals, samples were flash-frozen. Baseline correction of the raw data was done in Origin 2023, version 10.0.0.154. The spin concentration of peptide samples was calculated from double spectral integration. Due to extensive superhyperfine features, reliable spin integrations were not obtained for 4SCC.

EPR simulations were done in EasySpin 6.0.0[91] using the MATLAB (R2024a) interface. An axial g tensor was used for Cu with the appropriate number of ^{14}N nuclei (3 for trimer and 4 for tetramer). The hyperfine tensor Aframe was invoked to transfer the molecular frame to the A tensor. A Lorentzian line broadening was used. All simulations were done using the method suitable for frozen solutions (pepper).

Electrochemistry

All electrochemistry experiments were performed using a Wave Driver 20 bi-potentiostat (Pine Research) with PGE as the working electrode, a coiled platinum wire as the counter electrode, and Ag/AgCl (in

saturated KCl) as the reference electrode. The potential values were referenced against Ag/AgCl and converted to SHE. Temperature-dependent experiments were done in an RRDE cell with a water jacket by controlling the temperature from a circulating water bath.

i. λ_T determination

The RDE experiments were used to determine the total reorganization energy, λ_T. All RDE experiments were performed with 0.25 mM ArCuPs dissolved in 80 mM mixed buffer, pH 6.5, and 100 mM KCl as a supporting electrolyte under anaerobic conditions. RDE experiments (Fig. 6B, S15, S16, S24) show an increase in the current with an increase in rotation rates following the Koutecký-Levich (K-L) relationship, Eq. (ii)[92], with i_L and i_K representing the Levich current and kinetic currents, respectively. Here, n is the number of electrons transferred during the redox process, F is Faraday's constant 96485 C mol^{-1}, A = area of the electrode (0.19625 cm^2), C_0 is the concentration of ArCuP (0.25 mM), and Γ is the surface coverage of the electrode (88 ± 8 $\times 10^{-12}$ mol cm^{-2}). k_{ET} is the ET rate constant (k_{ET} in $M^{-1}s^{-1}$). D_0 is the diffusion coefficient of the analyte, ω is the angular velocity of the electrode, and ν is the kinematic viscosity of the solution.

$$\frac{1}{i} = \frac{1}{i_L} + \frac{1}{i_K} = \frac{1}{0.62nFAC_0(D_0)^{2/3}\upsilon^{-1/6}\omega^{1/2}} + \frac{1}{nFAC_0k_{ET}\Gamma} \qquad \text{(ii)}$$

From the intercepts of the linear i^{-1} vs. $\omega^{-1/2}$ plots, the second-order rate constant for ET (k_{ET}) was determined given that in the absence of other competing chemical/redox phenomena, the only process occurring is the ET. The k_{ET} was obtained at five different potentials in the mass transport-limited region between −0.05 V and 0.4 V. The experiments were performed at three different temperatures, and for each temperature, k_{ET} was determined (Table S4, S5, S10). λ_T was obtained from the slopes of $\ln(k_{ET}T^{-1/2})$ vs. T^{-1} plots (Fig. 6C, S15, S16, S24) according to the Arrhenius Eq. (iii).

$$\lambda = -4.03\, d\,ln\left(kT^{-\frac{1}{2}}\right)/d[T^{-1}) \qquad \text{(iii)}$$

ii. $\lambda_{Cu\text{-}P}$ determination

The CV and CA experiments were performed with ten µL of 0.25 mM ArCuPs drop-cast on PGE and six µL of 0.1 M polymyxin B to facilitate electrostatic interaction between the ArCuPs and the electrode. The protein solution was then dried under N_2, and data were recorded in N_2-saturated 20 mM mixed buffers. Each CA experiment was performed for a total duration of 0.3 s (Fig. S18). Temperature-dependent CV and CA experiments were performed at seven different temperatures between 280 K and 310 K with 5 K increments. CVs were recorded to extract E°'s (Fig. S17, S23; Table S6, S9) and determine the overpotentials (η) at each temperature. Six different η were chosen, three on the cathodic (−150 mV, −100 mV, −50 mV) and three on the anodic (50 mV, 100 mV, 150 mV) side of E°'s at each temperature. At a given η, the current follows an exponential relationship with time according to Eq. (iv)

$$i = k_{app}\, Q \exp(-k_{app}t) \qquad \text{(iv)}$$

where k_{app} is the apparent ET rate constant in s^{-1}, Q is the total charge passed during CA, and t is the time. The decay current consists of the charging current and the Faradaic current. The capacitive current decayed within 1 ms for the blank electrode at pH 6.5. To avoid the charging current decaying completely from the Faradaic response, ln(i) vs. t plots (Fig. 6E, S19, S20, S25) were constructed beyond the decay time for the blank electrode. From the slope of these semi-logarithmic graphs, the heterogeneous ET rates k_{app} (s^{-1}) (Table S7, S8, S11) were determined at each temperature and η, which was used to calculate λ. Arrhenius plots of $\ln(k_{app}T^{-1/2})$ vs. T^{-1} were made (Fig. S21, S22, S26) using k_{app} from above[93]. The $\lambda_{Cu\text{-}P}$ at each η was calculated from the slopes of these plots.

Data availability

The coordinates and structure factors have been deposited in the Protein Data Bank with accession codes 8VHS for 4SCC and 9BQR for K6E/E8K-4SCC. All other data presented in this study are available from the corresponding author upon request. Source data are provided with this paper.

References

1. Liu, J. et al. Metalloproteins containing cytochrome, iron–sulfur, or copper redox centers. *Chem. Rev.* **114**, 4366–4469 (2014).
2. Van Stappen, C. et al. Designing artificial metalloenzymes by tuning of the environment beyond the primary coordination sphere. *Chem. Rev.* **122**, 11974–12045 (2022).
3. Koebke, K. J., Pinter, T. B., Pitts, W. C. & Pecoraro, V. L. Catalysis and electron transfer in de novo designed metalloproteins. *Chem. Rev.* **122**, 12046–12109 (2022).
4. Winkler, J. R. & Gray, H. B. Electron flow through metalloproteins. *Chem. Rev.* **114**, 3369–3380 (2014).
5. Moser, C. C., Keske, J. M., Warncke, K., Farid, R. S. & Dutton, P. L. Nature of biological electron transfer. *Nature* **355**, 796–802 (1992).
6. Solomon, E. I. et al. Copper active sites in biology. *Chem. Rev.* **114**, 3659–3853 (2014).
7. Ciano, L., Davies, G. J., Tolman, W. B. & Walton, P. H. Bracing copper for the catalytic oxidation of C–H bonds. *Nat. Catal.* **1**, 571–577 (2018).
8. Adelson, C. N. et al. Characterization of the preprocessed copper site equilibrium in amine oxidase and assignment of the reactive copper site in topaquinone biogenesis. *J. Am. Chem. Soc.* **141**, 8877–8890 (2019).
9. Suzuki, S., Kataoka, K. & Yamaguchi, K. Metal coordination and mechanism of multicopper nitrite reductase. *Acc. Chem. Res.* **33**, 728–735 (2000).
10. Tsukihara, T. et al. Structures of metal sites of oxidized bovine heart cytochrome c oxidase at 2.8Å. *Science* **269**, 1069–1074 (1995).
11. Meier, K. K. et al. Oxygen activation by Cu LPMOs in recalcitrant carbohydrate polysaccharide conversion to monomer sugars. *Chem. Rev.* **118**, 2593–2635 (2018).
12. Kjaergaard, C. H. et al. Spectroscopic and computational insight into the activation of O_2 by the mononuclear Cu center in polysaccharide monooxygenases. *Proc. Natl Acad. Sci.* **111**, 8797 (2014).
13. Vaaje-Kolstad, G. et al. An oxidative enzyme boosting the enzymatic conversion of recalcitrant polysaccharides. *Science* **330**, 219–222 (2010).
14. Courtade, G. et al. Mechanistic basis of substrate-O(2) coupling within a chitin-active lytic polysaccharide monooxygenase: An integrated NMR/EPR study. *Proc. Natl Acad. Sci.* **117**, 19178–19189 (2020).
15. Forsberg, Z. et al. Polysaccharide degradation by lytic polysaccharide monooxygenases. *Curr. Opin. Struct. Biol.* **59**, 54–64 (2019).
16. Bissaro, B. et al. Oxidative cleavage of polysaccharides by monocopper enzymes depends on H_2O_2. *Nat. Chem. Biol.* **13**, 1123 (2017).
17. Bissaro, B. et al. Molecular mechanism of the chitinolytic peroxygenase reaction. *Proc. Natl Acad. Sci.* **117**, 1504–1513 (2020).
18. Hangasky, J. A., Iavarone, A. T. & Marletta, M. A. Reactivity of O_2 versus H_2O_2 with polysaccharide monooxygenases. *Proc. Natl Acad. Sci.* **115**, 4915–4920 (2018).
19. Jones, S. M., Transue, W. J., Meier, K. K., Kelemen, B. & Solomon, E. I. Kinetic analysis of amino acid radicals formed in H_2O_2-driven Cu(I) LPMO reoxidation implicates dominant homolytic reactivity. *Proc. Natl Acad. Sci.* **117**, 11916–11922 (2020).
20. Paradisi, A. et al. Formation of a copper (II)–tyrosyl complex at the active site of lytic polysaccharide monooxygenases following oxidation by H_2O_2. *J. Am. Chem. Soc.* **141**, 18585–18599 (2019).

21. Wang, B., Wang, Z., Davies, G. J., Walton, P. H. & Rovira, C. Activation of O_2 and H_2O_2 by lytic polysaccharide monooxygenases. *ACS Catal.* **10**, 12760–12769 (2020).
22. Balasubramanian, R. et al. Oxidation of methane by a biological dicopper centre. *Nature* **465**, 115–119 (2010).
23. Hakemian, A. S. & Rosenzweig, A. C. The biochemistry of methane oxidation. *Annu. Rev. Biochem.* **76**, 223–241 (2007).
24. Smith, S. M. et al. Crystal structure and characterization of particulate methane monooxygenase from *Methylocystis* species strain M. *Biochemistry* **50**, 10231–10240 (2011).
25. Ross, M. O. et al. Particulate methane monooxygenase contains only mononuclear copper centers. *Science* **364**, 566–570 (2019).
26. Tucci, F. J., Jodts, R. J., Hoffman, B. M. & Rosenzweig, A. C. Product analogue binding identifies the copper active site of particulate methane monooxygenase. *Nat. Catal.* **6**, 1194–1204 (2023).
27. Koo, C. W., Tucci, F. J., He, Y. & Rosenzweig, A. C. Recovery of particulate methane monooxygenase structure and activity in a lipid bilayer. *Science* **375**, 1287–1291 (2022).
28. Liew, E. F., Tong, D., Coleman, N. V. & Holmes, A. J. Mutagenesis of the hydrocarbon monooxygenase indicates a metal centre in subunit-C, and not subunit-B, is essential for copper-containing membrane monooxygenase activity. *Microbiology* **160**, 1267–1277 (2014).
29. Kim, B. et al. Fenton-like chemistry by a copper(I) complex and H_2O_2 relevant to enzyme peroxygenase C–H hydroxylation. *J. Am. Chem. Soc.* **145**, 11735–11744 (2023).
30. Kim, S. et al. Amine oxidative N-dealkylation via cupric hydroperoxide Cu-OOH homolytic cleavage followed by site-specific fenton chemistry. *J. Am. Chem. Soc.* **137**, 2867–2874 (2015).
31. Kakuda, S., Peterson, R. L., Ohkubo, K., Karlin, K. D. & Fukuzumi, S. Enhanced catalytic four-electron dioxygen (O_2) and two-electron hydrogen peroxide (H_2O_2) reduction with a copper (II) complex possessing a pendant ligand pivalamido group. *J. Am. Chem. Soc.* **135**, 6513–6522 (2013).
32. Maiti, D., Narducci Sarjeant, A. A. & Karlin, K. D. Copper (II)–hydroperoxo complex induced oxidative N-dealkylation chemistry. *J. Am. Chem. Soc.* **129**, 6720–6721 (2007).
33. Yu, F. et al. Protein design: Toward functional metalloenzymes. *Chem. Rev.* **114**, 3495–3578 (2014).
34. Korendovych, I. V. & DeGrado, W. F. De novo protein design, a retrospective. *Q. Rev. Biophys.* **53**, E3 (2020).
35. Lombardi, A., Pirro, F., Maglio, O., Chino, M. & DeGrado, W. F. De novo design of four-helix bundle metalloproteins: One scaffold, diverse reactivities. *Acc. Chem. Res.* **52**, 1148–1159 (2019).
36. Beesley, J. L. & Woolfson, D. N. The de novo design of α-helical peptides for supramolecular self-assembly. *Curr. Opin. Biotech.* **58**, 175–182 (2019).
37. Fletcher, J. M. et al. A basis set of de novo coiled-coil peptide oligomers for rational protein design and synthetic biology. *ACS Synth. Biol.* **1**, 240–250 (2012).
38. Woolfson, D. N. A brief history of de novo protein design: Minimal, rational, and computational. *J. Mol. Biol.* **433**, 167160 (2021).
39. Tegoni, M., Yu, F., Bersellini, M., Penner-Hahn, J. E. & Pecoraro, V. L. Designing a functional type 2 copper center that has nitrite reductase activity within α-helical coiled coils. *Proc. Natl Acad. Sci.* **109**, 21234–21239 (2012).
40. Zastrow, M. L., Peacock, A. F. A., Stuckey, J. A. & Pecoraro, V. L. Hydrolytic catalysis and structural stabilization in a designed metalloprotein. *Nat. Chem.* **4**, 118–123 (2012).
41. Faiella, M. et al. An artificial di-iron oxo-protein with phenol oxidase activity. *Nat. Chem. Biol.* **5**, 882–884 (2009).
42. Reig, A. J. et al. Alteration of the oxygen-dependent reactivity of de novo due ferri proteins. *Nat. Chem.* **4**, 900–906 (2012).
43. Koebke, K. J. et al. Modifying the steric properties in the second coordination sphere of designed peptides leads to enhancement of nitrite reductase activity. *Angew. Chem. Int. Ed.* **57**, 3954–3957 (2018).
44. Pirro, F. et al. A de novo-designed type 3 copper protein tunes catechol substrate recognition and reactivity. *Angew. Chem. Int. Ed.* **62**, e202211552 (2023).
45. Mitra, S. et al. De novo design of a self-assembled artificial copper peptide (ArCuP) that activates and reduces peroxide. *ACS Catal.* **11**, 10267–10278 (2021).
46. Prakash, D., Mitra, S., Murphy, M. & Chakraborty, S. Oxidation and peroxygenation of C–H bonds by artificial Cu peptides (ArCuPs): Improved catalysis via selective outer sphere modifications. *ACS Catal.* **12**, 8341–8351 (2022).
47. Malayam Parambath, S. et al. A de novo-designed artificial metallopeptide hydrogenase: Insights into photochemical processes and the role of protonated cys. *ChemSusChem* **14**, 2237–2246 (2021).
48. Prasad, P. et al. Photocatalytic hydrogen evolution by a de novo designed metalloprotein that undergoes Ni-mediated oligomerization shift. *Chem. Eur. J.* **29**, e202202902 (2023).
49. Harbury, P. B., Zhang, T., Kim, P. S. & Alber, T. A switch between two-, three-, and four-stranded coiled coils in GCN4 leucine zipper mutants. *Science* **262**, 1401–1407 (1993).
50. Ohta, T., Tachiyama, T., Yoshizawa, K. & Yamabe, T. Synthesis, structure, and catalytic function of a disulfide-bridged dicopper(I) complex. *Tetrahedron. Lett.* **41**, 2581–2585 (2000).
51. Osako, T., Nagatomo, S., Tachi, Y., Kitagawa, T. & Itoh, S. Low-temperature stopped-flow studies on the reactions of copper(II) complexes and H_2O_2: The first detection of a mononuclear copper(II)–peroxo intermediate. *Angew. Chem. Int. Ed.* **41**, 4325–4328 (2002).
52. Fujii, T. et al. Construction of a square-planar hydroperoxo-copper(II) complex inducing a higher catalytic reactivity. *Chem. Commun.* 2700–2701 https://doi.org/10.1039/b308073k (2003).
53. Kim, S., Saracini, C., Siegler, M. A., Drichko, N. & Karlin, K. D. Coordination chemistry and reactivity of a cupric hydroperoxide species featuring a proximal H-bonding substituent. *Inorg. Chem.* **51**, 12603–12605 (2012).
54. Elwell, C. E. et al. Copper–oxygen complexes revisited: Structures, spectroscopy, and reactivity. *Chem. Rev.* **117**, 2059–2107 (2017).
55. Liu, Y., Harnden, K. A., Van Stappen, C., Dikanov, S. A. & Lu, Y. A designed copper histidine-brace enzyme for oxidative depolymerization of polysaccharides as a model of lytic polysaccharide monooxygenase. *Proc. Natl Acad. Sci.* **120**, e2308286120 (2023).
56. Hirst, J. Elucidating the mechanisms of coupled electron transfer and catalytic reactions by protein film voltammetry. *Biochim. Biophys. Acta* **1757**, 225–239 (2006).
57. Marcus, R. A. Chemical and electrochemical electron-transfer theory. *Ann. Rev. Phys. Chem.* **15**, 155–196 (1964).
58. Marcus, R. A. On the theory of oxidation-reduction reactions involving electron transfer. I. *J. Chem. Phys.* **24**, 966–978 (1956).
59. Marcus, R. A. & Sutin, N. Electron transfers in chemistry and biology. *Biochim. Biophys. Acta* **811**, 265–322 (1985).
60. Di Bilio, A. J. et al. Reorganization energy of blue copper: Effects of temperature and driving force on the rates of electron transfer in ruthenium- and osmium-modified azurins. *J. Am. Chem. Soc.* **119**, 9921–9922 (1997).
61. Farver, O. & Pecht, I. Electron transfer in blue copper proteins. *Coord. Chem. Rev.* **255**, 757–773 (2011).
62. Murgida, D. H. & Hildebrandt, P. Electrostatic-field dependent activation energies modulate electron transfer of cytochrome c. *J. Phys. Chem. B* **106**, 12814–12819 (2002).
63. Chattopadhyay, S. et al. Contributions to cytochrome c inner- and outer-sphere reorganization energy. *Chem. Sci.* **12**, 11894–11913 (2021).
64. Chidsey, C. E. D. Free energy and temperature dependence of electron transfer at the metal-electrolyte interface. *Science* **251**, 919–922 (1991).

65. Song, S., Clark, R. A., Bowden, E. F. & Tarlov, M. J. Characterization of cytochrome c/alkanethiolate structures prepared by self-assembly on gold. *J. Phys. Chem.* **97**, 6564–6572 (1993).
66. Lee, C. W. & Anson, F. C. Recalculation of the rate of electron exchange between copper (II) and copper (I) in their 1, 10-phenanthroline and 2, 2′-bipyridine complexes in aqueous media. *J. Phys. Chem.* **87**, 3360–3362 (1983).
67. Winkler, J. R., Wittung-Stafshede, P., Leckner, J., Malmström, B. G. & Gray, H. B. Effects of folding on metalloprotein active sites. *Proc. Natl Acad. Sci.* **94**, 4246–4249 (1997).
68. Margalit, R. et al. Preparation and characterization of pentaammineruthenium-(histidine-83)azurin: Thermodynamics of intramolecular electron transfer from ruthenium to copper. *Proc. Natl Acad. Sci.* **81**, 6554–6558 (1984).
69. Di Bilio, A. J. et al. Electron transfer in ruthenium-modified plastocyanin. *J. Am. Chem. Soc.* **120**, 7551–7556 (1998).
70. Farver, O. et al. Long-range electron transfer in engineered azurins exhibits Marcus inverted region behavior. *J. Phys. Chem. Lett.* **6**, 100–105 (2015).
71. Farver, O., Marshall, N. M., Wherland, S., Lu, Y. & Pecht, I. Designed azurins show lower reorganization free energies for intraprotein electron transfer. *Proc. Natl Acad. Sci.* **110**, 10536–10540 (2013).
72. Farver, O., Lu, Y., Ang, M. C. & Pecht, I. Enhanced rate of intramolecular electron transfer in an engineered purple Cu_A azurin. *Proc. Natl Acad. Sci.* **96**, 899–902 (1999).
73. Farver, O., Eady, R. R. & Pecht, I. Reorganization energies of the individual copper centers in dissimilatory nitrite reductases: Modulation and control of internal electron transfer. *J. Phys. Chem. A* **108**, 9005–9007 (2004).
74. Lancaster, K. M. et al. Electron transfer reactivity of type zero *Pseudomonas aeruginosa* azurin. *J. Am. Chem. Soc.* **133**, 4865–4873 (2011).
75. Lancaster, K. M., George, S. D., Yokoyama, K., Richards, J. H. & Gray, H. B. Type-zero copper proteins. *Nat. Chem.* **1**, 711–715 (2009).
76. Balland, V., Hureau, C. & Savéant, J.-M. Electrochemical and homogeneous electron transfers to the alzheimer amyloid-β copper complex follow a preorganization mechanism. *Proc. Natl Acad. Sci.* **107**, 17113–17118 (2010).
77. Zerk, T. J., Saouma, C. T., Mayer, J. M. & Tolman, W. B. Low reorganization energy for electron self-exchange by a formally copper(III,II) redox couple. *Inorg. Chem.* **58**, 14151–14158 (2019).
78. Cao, R. et al. Peroxo and superoxo moieties bound to copper ion: Electron-transfer equilibrium with a small reorganization energy. *J. Am. Chem. Soc.* **138**, 7055–7066 (2016).
79. Cascella, M., Magistrato, A., Tavernelli, I., Carloni, P. & Rothlisberger, U. Role of protein frame and solvent for the redox properties of azurin from *Pseudomonas aeruginosa*. *Proc. Natl Acad. Sci.* **103**, 19641–19646 (2006).
80. Kabsch, W. Xds. *Acta Crystallogr. D. Biol. Crystallogr.* **66**, 125–132 (2010).
81. Evans, P. R. & Murshudov, G. N. How good are my data and what is the resolution? *Acta Crystallogr. D. Biol. Crystallogr.* **69**, 1204–1214 (2013).
82. Zwart, P. H., Grosse-Kunstleve, R. W. & Adams, P. D. Phenix.Xtriage. *CCP4 Newsl. 43*, contribution **7** (2005).
83. McCoy, A. J. et al. Phaser crystallographic software. *J. Appl. Crystallogr.* **40**, 658–674 (2007).
84. Potterton, L. et al. CCP4i2: The new graphical user interface to the CCP4 program suite. *Acta Crystallogr. D. Biol. Crystallogr.* **74**, 68–84 (2018).
85. Zaccai, N. R. et al. A de novo peptide hexamer with a mutable channel. *Nat. Chem. Biol.* **7**, 935–941 (2011).
86. Cowtan, K. The Buccaneer software for automated model building. 1. Tracing protein chains. *Acta Crystallogr. D. Biol. Crystallogr.* **62**, 1002–1011 (2006).
87. Afonine, P. V. et al. Towards automated crystallographic structure refinement with phenix. Refine. *Acta Crystallogr. D. Biol. Crystallogr.* **68**, 352–367 (2012).
88. Emsley, P. & Cowtan, K. Coot: Model-building tools for molecular graphics. *Acta Crystallogr. D. Biol. Crystallogr.* **60**, 2126–2132 (2004).
89. Murshudov, G. N. et al. Refmac5 for the refinement of macromolecular crystal structures. *Acta Crystallogr. D. Biol. Crystallogr.* **67**, 355–367 (2011).
90. McNicholas, S., Potterton, E., Wilson, K. S. & Noble, M. E. M. Presenting your structures: The CCP4mg molecular-graphics software. *Acta Crystallogr. D. Biol. Crystallogr.* **67**, 386–394 (2011).
91. Stoll, S. & Schweiger, A. Easyspin, a comprehensive software package for spectral simulation and analysis in EPR. *J. Magn. Reson.* **178**, 42–55 (2006).
92. Nazemi, Z., Prasad, P. & Chakraborty, S. Kinetics of oxygen reduction by a beta barrel heme protein on hybrid bioelectrodes. *ChemElectroChem* **7**, 1029–1037 (2020).
93. Park, W.-c & Hong, H.-G. Determination of reorganization energy from the temperature dependence of electron transfer rate constant for hydroquinone-tethered self-assembled monolayers (SAMs). *Bull. Korean Chem. Soc.* **27**, 381–385 (2006).
94. Farver, O., Eady, R. R., Sawers, G., Prudêncio, M. & Pecht, I. Met144Ala mutation of the copper-containing nitrite reductase from Alcaligenes xylosoxidans reverses the intramolecular electron transfer. *FEBS Lett.* **561**, 173–176 (2004).

Acknowledgements

S.C. thanks the University of Mississippi for its support. Major funding for the Bruker EMXPlus was provided by the National Science Foundation Award 1726244 (2017) to the School of Chemical Sciences EPR lab at the University of Illinois. This research used resources of the Advanced Photon Source, a U.S. Department of Energy (DOE) Office of Science User Facility operated for the DOE Office of Science by Argonne National Laboratory under contract no. DE-AC02-06CH11357. The use of the LS-CAT Sector 21 was supported by the Michigan Economic Development Corporation and the Michigan Technology Tri-Corridor (Grant 085P1000817). Use of the Stanford Synchrotron Radiation Lightsource, SLAC National Accelerator Laboratory, is supported by the U.S. DOE, Office of Science, Office of Basic Energy Sciences under contract no. DE-AC02-76SF00515. The SSRL Structural Molecular Biology Program is supported by the DOE Office of Biological and Environmental Research and by the National Institutes of Health, National Institute of General Medical Sciences (P30GM133894). This research used resources of the National Synchrotron Light Source II, a U.S. DOE Office of Science User Facility operated for the DOE Office of Science by Brookhaven National Laboratory under contract no. DE-SC0012704. The Center for BioMolecular Structure (CBMS) is primarily supported by the National Institutes of Health, the National Institute of General Medical Sciences through a Center Core P30 Grant (P30GM133893), and by the DOE Office of Biological and Environmental Research (KP1605010).

Author contributions

S.C., D.P., and S.M. conceived the project. D.P., S.M., S.S., M.M., L.A., and P.P. performed the experiments. D.P. and S.C. analyzed the data. S.C. harvested the crystals, solved the X-ray structures, and refined the models. B.A. assisted with refining the K6E/E8K-4SCC structure. S.C. and D.P. wrote the manuscript, which other authors read and contributed to.

Competing interests

The authors declare no competing interests.

Additional information

Supplementary information The online version contains supplementary material available at https://doi.org/10.1038/s41467-025-57904-5.

Correspondence and requests for materials should be addressed to Saumen Chakraborty.

Peer review information *Nature Communications* thanks the anonymous reviewer(s) for their contribution to the peer review of this work. A peer review file is available.